EasyChair Preprint

№ 7515

Neutrino Effect on Gamma Radiation Emission from Radioactive Nuclides

Itzhak Orion

February 26, 2022

Neutrino effect on Gamma Radiation Emission from Radioactive Nuclides

Itzhak Orion

Department of Nuclear Engineering, Ben-Gurion University of the Negev, Beer-Sheva, Israel

Abstract

Several studies concerning changes in the decay constants of radioactive nuclides have demonstrated that solar flares can temporarily alter radioactive decay rates. This study sought to explore the effect of neutrinos on radioactive nuclei by constructing a radiation detection system that employs a radioactive source in front of a neutrino emission system. Proton cyclotron was chosen as the source of neutrino emitters. Responding to cyclotron operations, each of four detection systems registered gamma count rate decreases. The results of this study confirm that rises in neutrino flux affected the decay rates of the examined radioactive nuclides. Here we provide significant evidence that neutrinos affect the radioactive decay process. Neutrino detection is known to be very challenging due to the minuscule absorption in a stable nucleus. However, the study found that there is a greater probability of radionuclides interaction with the neutrino.

Keywords: Cyclotron, radioactive, neutrino, gamma, radiation

Introduction

Several studies have demonstrated that solar flares modify the radioactive decay constant. The change in the radioactive decay constant due to solar flares motivated us to seek the origins of this effect.

Researchers first observed anomalies in the decay of Mn-54 in 2006[1]. The resulting measurements demonstrated changes in the count rate of the gamma rays associated with the decay of the radionuclide, which undergoes a radioactive electron capture process by the nucleus. In radioactive decay, a stochastic process in an unstable nucleus determines a constant probability of particle emission. Every radioisotope emits particles in a unique process, with a specific decay constant expressed in units of disintegrations per second (Bq). The nucleus emits energy and releases nuclear radiation, meaning the release of gamma ray radiation, a beta-minus particle (electron), a beta-plus (positron), a neutron, an alpha particle, or a neutrino or an anti-neutrino. In certain cases of nuclear decay, the nucleus emits more than one particle at the same time, or in a chain of disintegration. The decay constant is considered a physical constant, according to measurements taken over the period during which the various radioisotopes decay[2]. The radioactive decay constant for a variety of isotopes ranges from 10^{6} sec^{-1} to 10^{-10} $year^{-1}$. The specific activity of the radionuclide is determined by multiplying the decay constant by Avogadro's constant divided by the molar mass.

Certain studies[3] have investigated whether the decay constant remains the same under all conditions. Jenkins' results concerning count rates of gamma radiation demonstrated a decrease over three different periods of time, with the changes occurring not as a result of statistical fluctuations but rather due to, among other factors, powerful solar flares (class X-M)[1]. Following this publication, scholars suggested that changes in the radioactive decay constant of Mn-54 result from a rise in the neutrino flux originating from the sun during solar flares. They discerned a correlation between the occurrence of a solar flare and changes in the decay rate of Mn-54. The nuclear activity that takes place in the sun is measured constantly by GOES series satellites, revealing power changes in the X rays that reach an orbital path around the earth. A solar flare is characterized by a rise in the intensity of the flux of elementary particles, including the neutrino.

The physicist W. E. Pauli hypothesized that the neutrino could offer a solution to the problem of balance of momentum and energy in beta decay. The neutrino, an elementary particle lacking charge, is emitted together with the electron from the nucleus in a process influenced by the weak nuclear force field[4]. This particle, a Fermion with a 1/2 spin and minimal mass (less than 0.2 eV), was presumed to be massless[5]; however, recent studies on different fronts have sought to establish its mass[6-7]. As early as 1958, Raymond Davis measured a neutrino using an inverted beta process in which the neutrino was captured by a stable Cl-37 nucleus close to a nuclear reactor that served as the source of anti-neutrinos[8], and in 1970, Davis established a detector using a tank of stable chlorine solution to measure the neutrinos originating from the sun[9-10].

The most recent estimations regarding solar neutrino flux are based on the total luminosity of the sun[11-12]. The estimated neutrino flux is distributed versus the neutrino energy; hence, the estimated flux strongly varies depending on the nuclear reaction that occurs. The proton-proton (pp) reaction in the sun emits low energy neutrinos with $\phi \sim 10^{10}$ (par. cm^{-2} sec^{-1}), and carbon-nitrogen-oxygen (CNO) reaction emits $\phi \sim 10^{8}$ (par. cm^{-2} sec^{-1}), resulting in higher energy neutrinos[13]. However, the experimental neutrino flux measurement is in the order of $\phi \sim 10^{6}$ (par. cm^{-2} sec^{-1})[10], and the CNO reaction emits $\phi \sim 10^{4}$ (par. cm^{-2} sec^{-1}).

Recently, scholars have conducted further intensive studies regarding neutrino measurements using different detectors[14-20], and it is expected that studies will achieve flux values with greater confidence.

Our previous measurements examined the gamma ray count rate stability of several radioactive sources over a certain period[21-22]. We constructed a measurement system consisting of a detector shielded by 5-cm thick Lead that isolated the detector from background radiation. The laboratory temperature was controlled to ensure that count rate changes did not result from environmental conditions. In October 2018, a number of solar flares took place. During these solar flares, we measured the count rate of gamma rays from a radioactive source, Am-241. Three decreases in the readings were measured at first, and we found that these fit with the occurrence of the solar flares[21]. In the following months, further solar flares occurred, resulting in decreases that our counting system registered. Following these results in the measurement of gamma ray

emission from an Am-241 source, we established further systems to measure gamma radiation from an Rn-222 source[23], as well as Mn-54 and Co-57 sources[22]. Several solar flares took place, and in accordance we detected decreases in the count rates of gamma radiation of Rn-222, Mn-54, and Co-57 sources. Based on the isolation of the system, the only remaining possible explanation for these decreases is a neutrino penetrating the system. Considering these measurements, we suggest that the source of the decrease in count rate is the rise in neutrino flux during solar flares.

To examine this hypothesis, we decided to test a source that is liable to emit neutrinos in a controlled manner, similar to the Davis' method[24-25]. We chose to place the gamma rays measurement system in front of an18 MeV medical proton cyclotron.

2. Results and Discussion

This section presents the measurement results obtained from each of the four radioisotopes: Am-241, Rn-222, Thorium, and Co-57. Each measurement system consists of a 5.08 cm diameter and 5.08 cm length NaI(Tl) detector facing a radioactive source that tracks total counts at defined time intervals. The NaI(Tl) detector was operated in a total counting mode above 40 keV. The background gamma counts were ~130 cpm (counts per minute).
Neutrino flux is emitted from the two cyclotrons, which are located at around 20 m and at around 40 m from the measurement system, as shown in Figure 7. The results were obtained following the operation of two cyclotrons.

2.1 Am-241 system

The Am-241 source, with activity of around 37 kBq, yielded the following system measurement results.
After nine dual operations of the two cyclotrons, the Am-241 system showed nine separate count rate decreases. The counts were collected at intervals of 60 minutes by the detector. Table 1 summarizes the results for all nine dips in Am-241 counts.

Figure 1 provides an example of a sharp dip in Am-241 counts as a result of the neutrinos emitted by the cyclotrons.

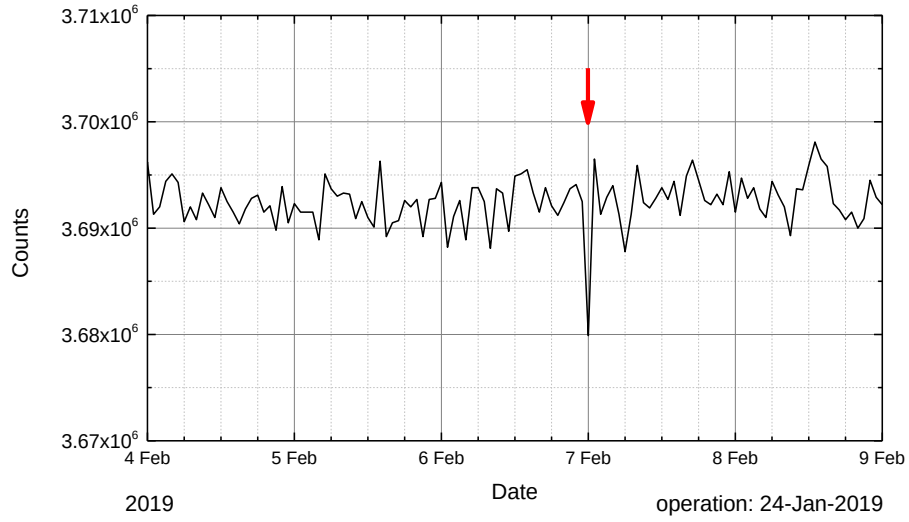

Figure 1. Am-241 count rate results. The red arrow indicates the Am-241 dip due to neutrinos emitted from the cyclotrons.

Date of cyclotron operation	Date of sharp dip	Delay (days)	Count decrease percentage
24-Jan-2019	06-Feb-2019	13	-0.38%
06- Feb-2019	19- Feb-2019	13	-0.27%
19 Feb-2019	04-Mar-2019	13	-0.24%
04-Mar-2019	17-Mar-2019	13	-0.28%
18-Mar-2019	29-Mar-2019	11	-0.29%
28-Mar-2019	12-Apr-2019	12	-0.30%
15-Apr-2019	26-Apr-2019	11	-0.21%
29-Apr-2019	12-May-2019	13	-0.22%
14-May-2019	28-May-2019	15	-0.26%

Table 1. Dual cyclotron operations summary and the corresponding Am-241 system responses.

To verify signal detectability and the reliability of the Am-241 results, we implemented the 'limits-of-detectability' method: "There is a 95% probability that a random sample will lie below the mean plus 1.645σ"[26]. Dips Critical level (L_C) was calculated using the neighboring counts average. Subsequently, dip counts were

compared to the $L_{C.}$ Once the presented dip counts were below the L_C value, it was clear that a reliable signal was detected and thus could be accepted as a valid result. Statistical significance calculations were performed (details in Supplementary information): $\%L_C = 0.11\%$; $\%\sigma = 0.049\%$.

According to the results, if a change is greater than $|0.11|\%$, the signal exceeded the critical level, and it is a reliable result. We obtained a signal of 7.75σ from the mean of Am-241 counts. Repetition and uniformity are evident in all nine dips—the percentage of decrease in the reading is higher than 0.11%. Therefore, all nine dips are considered statistically significant.

2.2 Rn-222 system

Thirteen dips in Rn-222 count rates were observed, responding to dual cyclotron operations. The 100 kBq Rn-222 activity (and its progeny) was continuously produced by a Ra-226 source placed in a freezer at - 40° C. The data was collected from the NaI(Tl) detector at 15 minute intervals. The dip results are summarized in Table 2. Figure 2 shows two examples of changes in Rn-222 count rates.

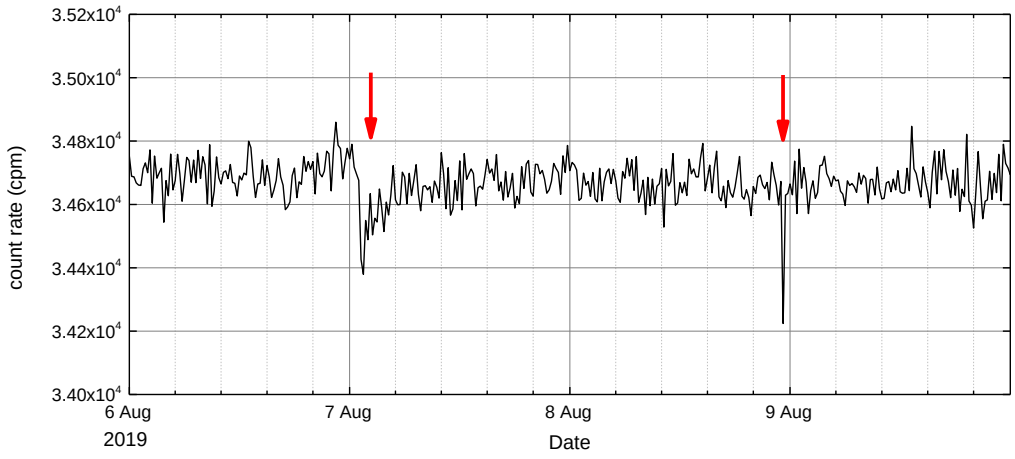

Figure 2. Rn-222 count rate system. The red arrows indicate the dips in Rn-222 due to neutrinos emitted from the cyclotrons.

Cyclotron operation time	Sharp dip time	Delay (Hr)	Count decrease percentage
01-Aug-2019 08:20	01-Aug-2019 13:00	05:30	-0.53%
06-Aug-2019 14:00	07-Aug-2019 01:30	11:30	-0.77%
08-Aug-2019 04:00	08-Aug-2019 23:15	19:15	-1.30%
25-Sep-2019 07:15	25-Sep-2019 23:15	16:00	-1.15%
18-Nov-2019 10:00	18-Nov-2019 23:15	13:15	-1.13%
19-Nov-2019 08:00	19-Nov-2019 20:00	12:00	-0.48%
21-Nov-2019 02:00	21-Nov-2019 13:30	11:30	-0.71%
21-Nov-2019 11:30	21-Nov-2019 23:45	12:15	-0.62%
26-Nov-2019 16:45	27-Nov-2019 07:15	14:30	-0.74%
16-Dec-2019 10:00	16-Dec-2019 22:15	12:15	-0.70%
24-Dec-2019 14:30	25-Dec-2019 23:15	8:45	-1.03%
26-Jan-2020 11:00	26-Jan-2020 23:15	12:15	-1.08%
02-Feb-2020 12:50	02-Feb-2020 23:15	10:25	-2.17%

Table 2. Summary of all cyclotron operations and Rn-222 system responses.

Statistical significance calculation results, using the 'limits-of-detectability' method, as described in the Supplementary information, are as follows: $\%L_C = 0.41\%$; $\%\sigma = 0.176\%$.

According to this, when the change in the count rate is greater than $|0.41|\%$, the dip is considered valid.

Using the same method as applied to Am-241, we detected a signal of 7.38σ from the mean of Rn-222 counts. Repetition and uniformity are evident in all registered dips—the percentage of decrease in readings is higher than 0.41%. Therefore, all dips presented in Table 2 are considered statistically significant.

2.3 Thorium system

Six operations of the cyclotrons triggered six decreases in the gamma count rate of the system. Thorium, in the form of $Th(NO_3)_4$, is a naturally occurring radioactive material (with its progeny) with about 500 kBq. Figure 3 shows an example of a decrease in counts due to cyclotron operation. Simultaneously, we performed similar measurements using an identical Thorium source and an identical detector at a control lab more than 50 km away from a cyclotron. The measurements yielded by the two systems, one near a cyclotron and one far from it, are presented in Supplementary information, Figure 9, and indicated that the dip occurred only in the system near the

cyclotron. This comparison confirms that the detected dip originated solely from the cyclotron operation.

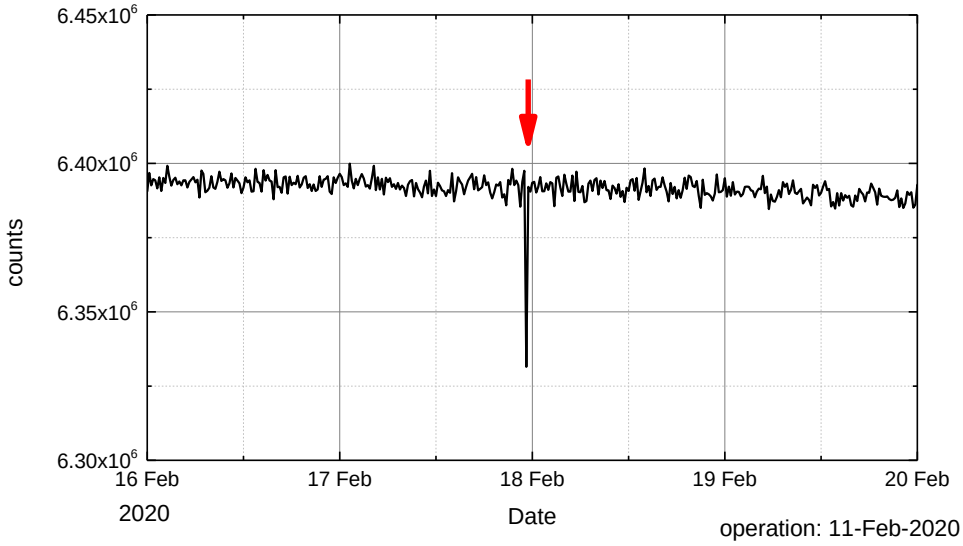

Figure 3. Thorium counts results. Dip is indicated by a red arrow.

Thorium results are presented in Table 3.

Date of cyclotron operation	Date of sharp dip	Delay (days)	Count decrease percentage
11-Feb-2020	17-Feb-2020	7	-0.97%
23-Feb-2020	02-Mar-2020	9	-1.06%
10-Mar-2020	19-Mar-2020	10	-0.98%
02-Apr-2020	14-Apr-2020	13	-1.07%
22-Apr-2020	03-May-2020	12	-1.05%
14-May-2020	23-May-2020	10	-0.99%

Table 3. Summary of cyclotron operations and resulting Thorium system responses.

For Thorium the statistical calculations (as in Supplementary information) obtained was: $\%L_C = 0.14\%$; $\%\sigma = 0.060\%$

The typical Thorium dip was 17.8σ from the mean. Repetition and uniformity are evident in all registered dips—the percentage of decrease in the reading is higher than 0.14%. Therefore, all dips presented in Table 3 are considered statistically significant.

Co-57 system

Twelve decreases in Co-57 counts were detected following twelve operations of the cyclotrons, as listed in Table 4. Figure 4 presents one example of the Co-57 response to neutrinos emitted from cyclotron operation.

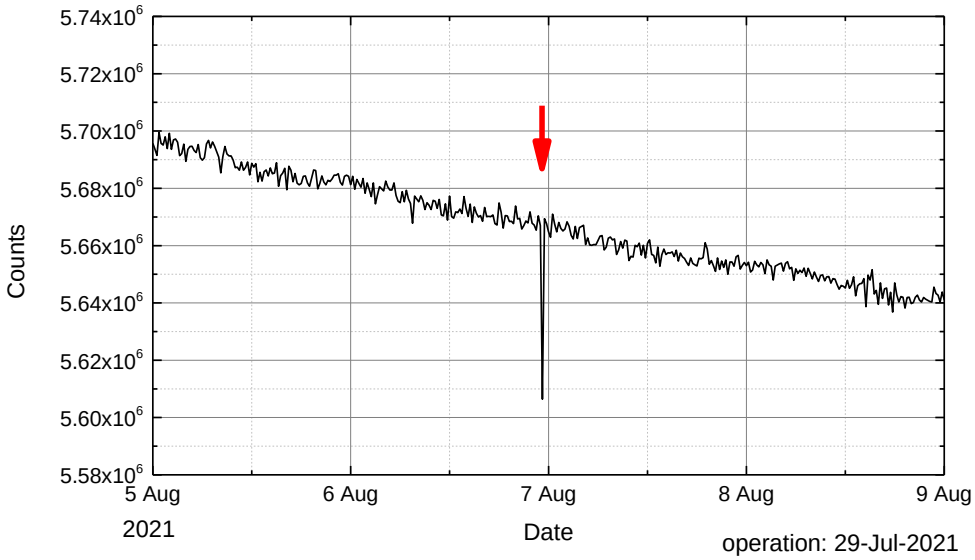

Figure 4. Co-57 counts showing a dip. Red arrow indicates a decrease in counts.

Date of cyclotron operation	Date of sharp dip	Delay (days)	Count decrease percentage
07-Jul-2020	12-Jul-2020	5	-1.06%
29-Jul-2020	06-Aug-2020	9	-1.07%
25-Aug-2020	31-Aug-2020	7	-1.02%
24-Sep-2020	27-Sep-2020	4	-0.95%
13-Oct-2020	20-Oct-2020	8	-0.98%
08-Dec-2020	14-Dec-2020	7	-1.12%
21-Dec-2020	27-Dec-2020	7	-1.10%
31-Dec-2020	08-Jan-2021	9	-1.20%
14-Jan-2021	20-Jan-2021	6	-1.06%
19-Jan-2021	25-Jan-2021	6	-1.63%
01-Feb-2021	06-Feb-2021	5	-1.07%
09-Feb-2021	18-Feb-2021	9	-0.96%

Table 4. Summary of all Co-57 system responses to cyclotron operations.

The measurements for Co-57 counts demonstrate a downward gradient because the source decays relatively rapidly due to its half-life of 272 days. Trapezoidal area calculation ($S_{\text{Trapezoidal}}$) of Co-57 was performed in order to obtain statistical confidence for our results. Data points were averaged on both sides around the count decrease that occurred on 06-Aug-2020, as shown in Figure 4, the average counts of both sides are required, to reduce regular fluctuations from readings[26]. Calculations for Co-57 obtained: $\%L_C = 0.098\%$; $\%\sigma = 0.042\%$. Therefore, we obtained a signal of 25σ from the mean of Co-57 counts. Repetition and uniformity are evident in all twelve dips—the percentage of decrease in reading is higher than 0.098%. Hence, all twelve dips are considered statistically significant.

Table 5 summarizes all the statistical considerations for the results of each radiation system.

Source	Change	σ	Number of σ Range
Am-241	(-0.21)-(-0.38)%	0.049%	4.3-7.7
Rn-222	(-0.48)-(-2.17)%	0.176%	2.7-12.3
Thorium	(-0.97)-(-1.07)%	0.060%	16.2-17.8
Co-57	(-0.95)-(-1.63)%	0.042%	22.6-33.8

Table 5. Range of the count rate change measured by each radiation system, and the results' statistical significance.

Rn-222 (and progeny) and thorium (and progeny) were used in our measurement systems; both these sources have a decay chain that consists of alpha or beta(-) emissions. The system of these experiments detects the gamma radiation from the overall decay chain emission. Therefore, at this stage we could not distinguish which emission was suppressed.

Am-241 decays to Np-237, which is a long half-life isotope. Therefore, in the Am-241 spectrum (above 40 keV), our system can only detect the 60 keV of Am-241. Thus, our finding corresponds only to the Am-241 disintegration.

Co-57 decays to stable Fe-57, and our system can only detect its gamma radiation emission. Therefore, our results indicated only the Co-57 decay decrease.

The results for the four radioisotopes indicate that gamma radiation count rates were suppressed. In two radioisotopes, the decrease is direct via the prime decay, while in the case of the two other radioisotopes, the decrease can be related to other decays along the decay chain, in alpha or betta emissions.

From the range of σ for each source, we found that Co-57 and thorium systems exhibited a much more significant response to the change in cyclotron neutrino flux.

The count rate decrease results indicate that a growth in neutrino flux alters the decay rates of the radioactive processes in four different radionuclides. The nuclear decay process was modified due to neutrino interaction with unstable nuclei.

3. Conclusion

Several studies of radioactive nuclei have indicated that solar flares modify the radioactive decay constant. Yet, there was doubt regarding what factor in the solar flares affected the change in radioactive decay constant.

Proton cyclotrons produce several types of radionuclides that emit neutrinos along with their decay, with a relatively high rate during a short period, around one hour or less. Therefore, the cyclotron provides a controlled and predicted neutrino source. Since the measurement system was placed close to the cyclotrons, it is certain that only electron-neutrinos reached the system.

In this study, repetitions were conducted for each measurement system to assure the validity of the results, and the attribution of the observed effect. Based on this study, we conclude that decreases in the decay rates for all the radioactive sources measured are due to an increase in the neutrino flux that penetrated the nucleus.

It is well known that neutrino detection is usually a very intricate task involving large stable matter detectors. However, in this study the neutrino interacted with an unstable

nucleus that could reveal different types of physical detection processes. The radioactive nucleus differs from a stable nucleus in that it has a nucleon occupying the occupied in higher energy levels. We assume that in the case of a radioactive nucleus, a neutrino could be captured in the nucleus shell structure, and this may explain the count rate alteration. This phenomenon indicates that further modelling of nuclear processes should be considered in the case of unstable nuclei in which a neutrino may be included in the internal nucleon structure.

This study presents findings regarding the initial effect of the neutrino on radioactive nuclei. Therefore, the theoretical aspects and mechanism of the process have yet to be investigated.

Methods and basic principles

Gamma Radiation Measurements

Two main methods are used to detect gamma radiation: crystal scintillation that emits light in response to the radiation, and a solid-state diode that produces electron-holes when exposed to radiation. Currently, most detectors are available with mounted electronics, analyzer hardware, and operating-software.

The gamma radiation flux or intensity is attenuated in media due to the medium specific-density and thickness, depending on the photon's energy, as follows:

$$I_x = I_0 e^{-\left(\frac{\mu}{\rho}\right)\rho x} \qquad (1)$$

Where:

x – Thickness.

ρ - Density

$\left(\frac{\mu}{\rho}\right)$ – Mass attenuation coefficient (depended on photon energy).

The attenuation coefficient is affected by photon absorption or scattering. The equation above (Equation 1) is limited to one dimension, while in reality the

attenuation process occurs in 3-D geometry. Also, as in any other type of radiation, the flux decreases due to the law of the inverse square distance.

In matter, any photon absorption ends with a rise in the atomic electron's kinetic energy. The photo-electric effect in the atom is responsible for photon absorption with atomic electron release (ionization). Compton scattering is another process via which photons interact with electrons (free or bonded). A portion of the initial energy is transferred to the scattered electron, and an outgoing photon moves in a different direction. Pair-production is a process whereby there is a probability that photons at above twice the electron-rest-mass energy produce pairs of electron-positron, which will carry kinetic energy. The occurrence of pair-production terminates the photon travel. Photon elastic scattering (Rayleigh scattering) by atoms is unlikely to occur in gamma radiation and diminishes as photon energy increases.

Photons can be produced as secondary radiation in several cases: atomic level X-ray emission, charge-particles Bremsstrahlung, synchrotron radiation, and Cherenkov radiation. Photons may be produced in the detector's surroundings, and therefore they can also be detected.

Scintillators

Scintillators are mostly solid or liquid, making them much more efficient in detecting gamma radiation than ionization gas detectors. Scintillators can be used for spectrometry. The scintillation process consists of light-output from electron energy deposition in matter. The scintillator is transparent in light, and therefore a light sensor, such as a photocathode, collects the light to produce and transfer a current pulse throughout a photomultiplier.

The available scintillation materials are obviously not ideal. The ideal scintillation properties for radiation detection are: efficient charge particles kinetic energy conversion to light; the light output should be proportional to the deposited energy; short luminescence decay time in order to produce fast pulses; high optical quality enabling the usage of large detectors; transparency to the emitted light; an index of refraction similar to glass to allow coupling to a sensor[26].

The gamma radiation detection in scintillation material goes through the following steps:

1. Gamma ray absorption – molecular excitation
2. Luminescence – visible light emission
3. Light transference to the photocathode
4. Light absorption in the photocathode and electron emission
5. Electron multiplication by the photomultiplier
6. Transfer of charged pulses to amplifier
7. Pulses tally in a counter or in a multi-plus-counting-analyzer (MCA).

The theoretical explanation of the scintillation process can be described based on the atomic energy levels of the scintillator crystal. Figure 5 illustrates the inorganic crystal scintillation process scheme.

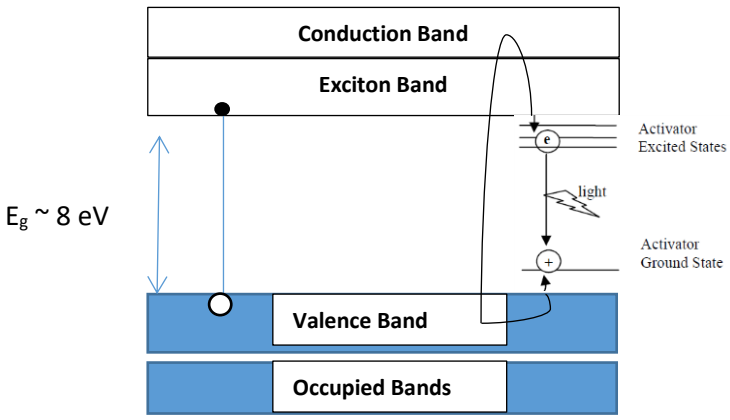

Figure 5. The electron band structure of a scintillation process for an inorganic scintillator with an activator.

First, gamma radiation interacts and an initial free electron is emitted. The initial electron causes secondary electrons to rise to the conduction band, leaving holes in the valence band. If the deposited energy is too low, an electrostatically coupled hole-electron is produced (electron at the exciton band). When the secondary electrons fall down to the valence band, electromagnetic radiation is emitted. These electromagnetic photons are in the optical wavelength range and can be detected by a photocathode. In the case of NaI(Tl) crystal, the energy gap between the valence band and the conduction band is too large for visible light emission; therefore, an activator is added

(impurity of Tl atoms) in order to insert more intermediate energy levels. Electrons and holes can jump to the activator levels, producing visible light emission via their recombination[27].

The light output of a scintillator directly depends on the efficiency related to the energy conversion from radiation into light photons. A fraction of the emitted light can be lost due to imperfections in the crystal's transparency and due to refraction. The fraction of the light passing through in good scintillators varies from 1/20 to 1/40. The overall efficiency is the average ionizing particle energy-loss for each photoelectron ejecting the cathode of the photomultiplier. In the photomultiplier, the amount of light translates linearly to charge. The number of electrons emitted from the photocathode is linearly dependent on gamma ray energy, absorbed energy fraction in the scintillator, efficiency of transfer energy to light, transparency to light, cathode field of view, and sensitivity to light wavelength. A fraction of electrons is collected by the dynodes in the photomultiplier. The outcome charge signal height depends on the number of electrons and on the photomultiplier multiplication.

In general, the photomultiplier tubes are devices that have a window in which a photocathode is mounted. Behind the photocathode is a collection optics area that leads electrons toward a series of dynodes to multiply the current pulse, ending at the anode. The tube is in a vacuum, and it is protected from magnetic fields. The range of photomultiplier types and materials is extremely vast, depending on the desired response. The overall schematic diagram of the electronic connection to the detector is presented in Figure 6.

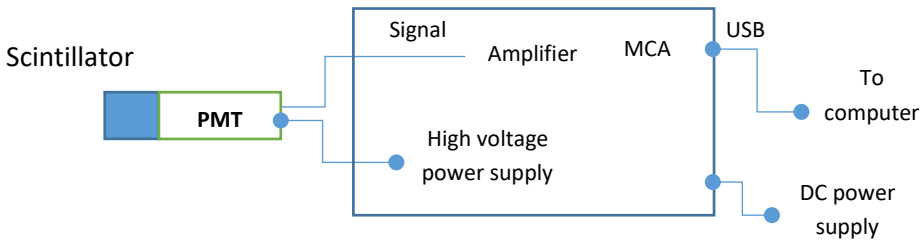

Figure 6 - Schematic diagram of a scintillator for gamma radiation spectrometry. The electronic devices are tiny and can be mounted on the PMT end.

Proton Cyclotron

To conduct a controlled examination of the effects of neutrinos on radioactive materials, a neutrino is produced using a cyclotron (proton accelerator).

A basic cyclotron contains a uniform magnetic field perpendicular to a vacuumed lattice in the shape of a disk divided into two equal sections (shaped as the letter “D”). The magnetic field causes the charged particles to move in a circular motion as a result of the Lorentz force. The acceleration is induced by a synchronized electric field in the gap between the two half-circle sections, when the particle passes through the gap. The particle’s radius of rotation increases as a result of the acceleration, hence making the particle trajectory spiral in shape[28]. Cyclotrons for proton acceleration were developed over the course of decades for use in nuclear research, and the proton final kinetic energy was gradually raised[29-30]. The basic structure of cyclotrons has also evolved[31]. A medical application of the proton cyclotron was developed for the production of radioactive agents to be used for imaging, such as the production of radioactive fluorine (F-18) for use in positron emission tomography (PET CT).

The cyclotron can be fitted with up to 8 targets for producing the most common PET radioisotopes.

$$^{18}_{8}O + p \rightarrow ^{18}_{9}F + n$$

$$^{18}_{9}F \rightarrow ^{18}_{8}O + \beta^{+} + \nu_e$$

IBA cyclotrons are operated with a current of protons that can reach up to 300 µA for protons at 18 MeV.

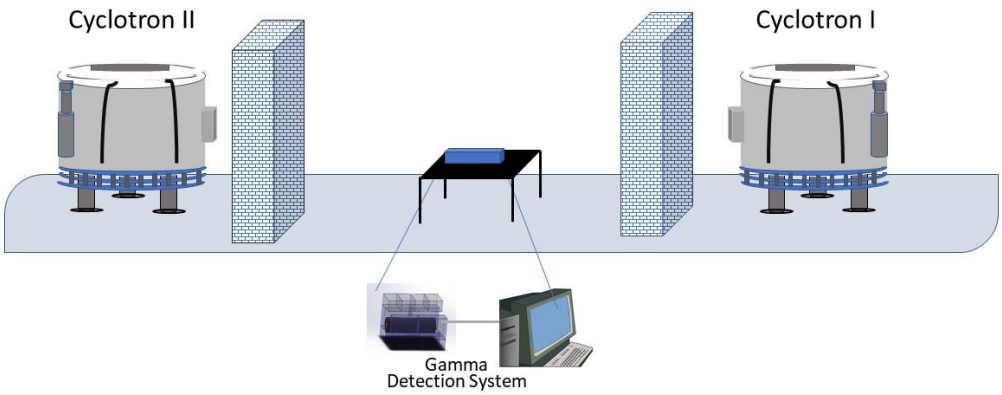

Figure 7. Schematic illustration of a radiation detection system with cyclotrons (dimensions not to scale).

Neutron emission from the cyclotron

Protons hit the target and subsequently neutrons are emitted. We closely positioned a KCl powder-based detector by the cyclotron walls. In the KCl, a fast neutron interacts with the chlorine and emits gamma radiation into an NaI(Tl) scintillator[32-33].

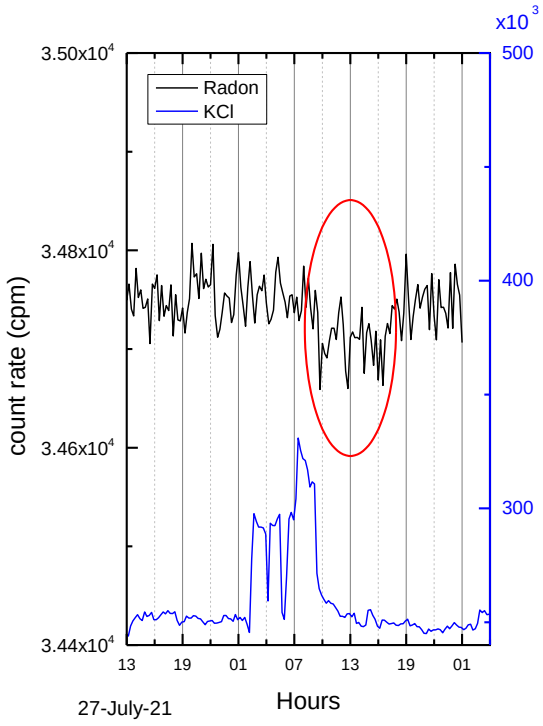

Figure 8. KCl detector system count rate response to fast neutrons from the cyclotron (blue line below); and the decrease in Rn-222 count rates following the cyclotron operation.

We performed two measurements in separate positions, one by the Rn-222 system and the other by the KCl detector system. The KCl system immediately responded to outgoing neutrons during the cyclotron operation, as shown in Figure 8, in the lower graph. The upper graph in Figure 8 presents the Rn-222 count rate data versus time. Figure 8 demonstrates that the Rn-222 decrease began around nine hours after the neutron emission. The whole decrease took about six hours due to a long cyclotron operation interval. A comparison of the two graphs indicates that cyclotron operation affected the Rn-222 count rate.

Activation

In a medical cyclotron, radionuclides are produced in the target and in surrounding structural materials. The radionuclides produced undergo Beta(+) emission or Electron Capture (EC) process. Therefore, in both cases a neutrino is emitted along with the process. Table 6 presents the theoretical production of these radionuclides with their yields per cyclotron current per hour, and $T_{1/2}$, from ref.[34-37].

Radionuclide	$T_{1/2}$	E_{max} (keV)	Thick Target Yield (MBq/μAh)
F-18	109.6 min	635	2960
Zn-63[35]	38.3 min	2344	2470[36]
Zn-65	245 day	330	0.2[37]
C-11	20.4 min	960	3820
N-13	10 min	1190	4440
O-15	122 s	1720	2220

Table 6. Theoretical radionuclide production in medical cyclotron based on previous studies[34-37].

Two cyclotrons were operated at the same time: Cyclotron-I at a distance of 25 m from the measurement system with 5.94 GBq/μAh, and Cyclotron-II at a distance of 40 m from the measurement system with 6.21 GBq/μAh. Cyclotron-I operated with currents up to 60 μA, and Cyclotron-II operated with currents around 75 μA, and dual cyclotron operations of two hours on average led to decreases.

Cyclotron-I:

Protons flux at activation port (Φ_p):

$$\Phi_p = 5.94\frac{GBq}{\mu A \cdot h} \cdot 2h \cdot 60\mu A = 713(GBq) = 7.13 \cdot 10^{11}\left(\frac{\#}{s}\right)$$

Distance dilution (d):

$$d = \frac{1}{r^2} = 1.6 \cdot 10^{-7}(cm^2)$$

F-18 production (P_{F-18}): 223 GBq (measured)

Neutrino from F-18 ($\Phi_{\upsilon_{F-18}}$):

$$\Phi_{\upsilon_{F-18}} = \frac{P_{F-18}}{d} = \frac{2.23 \cdot 10^{11}\left(\frac{\#}{s}\right)}{1.6 \cdot 10^{-7}(cm^2)} = 3.56 \cdot 10^4\left(\frac{\#}{s \cdot cm^2}\right)$$

Neutrino from N-13 production ($\Phi_{\nu_{N-13}}$):

$$\Phi_{\nu_{N-13}} \sim 5.4 \cdot 10^4\left(\frac{\#}{s \cdot cm^2}\right)$$

led to neutrino from CNO cycle with ($\Phi_{\nu_{CNO}}$):

$$\Phi_{\nu_{CNO}} \sim 3 \cdot \Phi_{\nu_{N-13}} = 3 \cdot 5.4 \cdot 10^4\left(\frac{\#}{s \cdot cm^2}\right) = 1.6 \cdot 10^5\left(\frac{\#}{s \cdot cm^2}\right)$$

Neutrino at measurement point (Φ_ν):

$$\Phi_\nu = \Phi_{\nu_{F-18}} + \Phi_{\upsilon_{CNO}} \sim 2 \cdot 10^5\left(\frac{\#}{s \cdot cm^2}\right)$$

Cyclotron-II:

Protons flux at activation port (Φ_p):

$$\Phi_p = 6.21\frac{GBq}{\mu A \cdot h} \cdot 2h \cdot 75\mu A = 931(GBq) = 9.31 \cdot 10^{11}\left(\frac{\#}{s}\right)$$

Distance dilution (d):

$$d = \frac{1}{r^2} = 6.25 \cdot 10^{-8}(cm^2)$$

F-18 production (P_{F-18}): 230 GBq (measured)

Neutrino from F-18 ($\Phi_{\nu_{F-18}}$):

$$\Phi_{\nu_{F-18}} = \frac{P_{F-18}}{d} = 1.44 \cdot 10^4 \left(\frac{\#}{s \cdot cm^2}\right)$$

Neutrino from N-13 production ($\Phi_{\nu_{N-13}}$):

$$\Phi_{\nu_{N-13}} \sim 2.2 \cdot 10^4 \left(\frac{\#}{s \cdot cm^2}\right)$$

led to neutrino from CNO cycle with ($\Phi_{\nu_{CNO}}$):

$$\Phi_{\nu_{CNO}} \sim 3 \cdot \Phi_{\nu_{N-13}} = 6.25 \cdot 10^4 \left(\frac{\#}{s \cdot cm^2}\right)$$

Neutrino at measurement point (Φ_ν):

$$\Phi_\nu = \Phi_{\nu_{F-18}} + \Phi_{\nu_{CNO}} \sim 8 \cdot 10^4 \left(\frac{\#}{s \cdot cm^2}\right)$$

Total neutrino at measurement point ($\Phi(total)_\nu$):

$$\Phi(total)_\nu = \Phi(cyclotron\_I)_\nu + \Phi(cyclotron\_II)_\nu \sim 2.8 \cdot 10^5 \left(\frac{\#}{s \cdot cm^2}\right)$$

During 15 min measurement the system was penetrated by total neutrinos (ν_{total}) :

$$\nu_{total} = \Phi(total)_\nu \cdot \Delta t \cdot A = 2.8 \cdot 10^5 \left(\frac{\#}{s \cdot cm^2}\right) \cdot 15(min) \cdot 60 \left(\frac{s}{min}\right) \cdot 1(cm^2)$$

$$\nu_{total} \sim 2.5 \cdot 10^8$$

Even more flux can be produced by other low abundance structural materials, such as Zn.

The total neutrino at measurement point is in a similar order of magnitude to typical solar neutrino flux.

Acknowledgements

We thank Dr. Rebecca Wolpe for the language editing of this manuscript.

Additional information

There is NO competing interest.

References

1. Jenkins, J. H. & Fischbach, E. Perturbation of nuclear decay rates during the solar flare of 2006 December 13. Astroparticle Physics 31(6), 407-411 (2009). https://doi.org/10.1016/j.astropartphys.2009.04.005.
2. Lapp, R. E. & Andrews, H. L. Nuclear Radiation Physics. Second Ed. p. 72. (Prentice-Hall Inc. 1954).
3. Alburger, D.E., Harbottle, G. & Norton, E.F. Half-life of32Si. Earth and Planetary Science Letters 78(2–3), 168-176 (1986). https://doi.org/10.1016/0012-821X(86)90058-0.
4. Holstein, B. R. Weak Interactions in Nuclei, (Princeton University Press, 2017). https://doi.org/10.1515/9781400887040
5. Reines, F. & Cowanjun., C. The Neutrino. Nature 178, 446–449 (1956). https://doi.org/10.1038/178446a0.
6. Capozzi, F., Lisi, E., Marrone, A. & Montanino, D. & Palazzo, A. Neutrino masses and mixings: Status of known and unknown 3ν parameters. Nuclear Physics B 908, 218-234 (2016). https://doi.org/10.1016/j.nuclphysb.2016.02.016.
7. Battye, R. A. & Moss, A. Evidence for Massive Neutrinos from Cosmic Microwave Background and Lensing Observations. Phys. Rev. Lett. 112(5), (2014). https://link.aps.org/doi/10.1103/PhysRevLett.112.051303
8. Davis, R., Harmer, D. S. & Hoffman, K. C. Search for Neutrinos from the Sun, Phys. Rev. Lett. 20 (21), 1205-1209 (1968). https://link.aps.org/doi/10.1103/PhysRevLett.20.1205.
9. Hampel, W. Particle physics: How to detect solar neutrinos. Nature 318, 312–313 (1985). https://doi.org/10.1038/318312a0.
10. Davis, R. A review of measurements of the solar neutrino flux and their variation, Nuclear Physics B - Proceedings Supplements 48(1–3), 284-298 (1996). https://doi.org/10.1016/0920-5632(96)00263-0.
11. Essig, R., Sholapurkar, M. & Yu, T. T. Solar neutrinos as a signal and background in direct-detection experiments searching for sub-GeV dark matter with electron recoils. Phys. Rev. D 97(9), (2018). https://link.aps.org/doi/10.1103/PhysRevD.97.095029
12. Gonzalez-Garcia, M.C., Maltoni, M. & Salvado, J. Direct determination of the solar neutrino fluxes from solar neutrino data. J. High Energ. Phys. 72, (2010). https://doi.org/10.1007/JHEP05(2010)072
13. The Borexino Collaboration. Experimental evidence of neutrinos produced in the CNO fusion cycle in the Sun. Nature 587, 577–582 (2020). https://doi.org/10.1038/s41586-020-2934-0
14. Kodama K. et al., Final tau-neutrino results from the DONuTexperiment, Physical Review D 78(5), 052002-1-20 (2008). https://link.aps.org/doi/10.1103/PhysRevD.78.052002.

15. Aartsen, M. G. et al. The IceCube Collaboration. Measurement of the multi-TeV neutrino interaction cross-section with IceCube using Earth absorption. Nature 551, 596–600 (2017). https://doi.org/10.1038/nature24459.
16. Goncharov M. et al., Precise Measurement of Dimuon Production Cross-Sections in ν_μ Fe and $\bar{\nu}_\mu$Fe Deep Inelastic Scattering at the Tevatron. Phys. Rev. D64(11), 112006-1-19 (2001). https://link.aps.org/doi/10.1103/PhysRevD.64.112006.
17. Stein, R., Velzen, S.v. & Kowalski, M. et al. A tidal disruption event coincident with a high-energy neutrino. Nat Astron 5, 510–518 (2021). https://doi.org/10.1038/s41550-020-01295-8.
18. Abreu H. et al. First neutrino interaction candidates at the LHC. Phys. Rev. D 104(9), L091101-1-7 (2021). https://link.aps.org/doi/10.1103/PhysRevD.104.L091101.
19. Halzen, F. & Kheirandish, A. Black holes associated with cosmic neutrino flares. Nat. Phys. 16, 498–500 (2020). https://doi.org/10.1038/s41567-020-0864-2.
20. Aprile E. et al. Observation of two-neutrino double electron capture in 124Xe with XENON1T. Nature 568, 532–535 (2019). https://doi.org/10.1038/s41586-019-1124-4.
21. Walg J., Rodnianski A., Orion I., Evidence of Neutrino Flux effect on Alpha Emission Radioactive Half-Life. ATINER's Conference Paper Proceedings Series PHY2019-0137 Athens, (2019).
22. Walg, J., Peleg, Y., Rodnianski, A. & Hazenshprung, N. & Orion, I. The Effect of Solar Flares on ^{54}Mn and ^{57}Co Radioactive Decay Constants Performance. Nuclear Technology & Radiation Protection 36(3), 219-223 (2021).
23. Walg J., Rodnianski A. & Orion I., Solar Flare Detection Method Using Rn-222 Radioactive Source. GSC Advanced Research and Reviews 05(02), 159–166 (2020). https://doi.org/10.30574/gscarr.2020.5.2.0087.
24. Davis, R. Jr., Evans, J. C. & Cleveland, B. T. The solar neutrino problem. AIP Conference Proceedings 52, 17-27 (1979). https://doi.org/10.1063/1.31802.
25. Davis, R. Jr., Evans, J. C. & Cleveland, B. T. Proc. Conf. Neutrinos, 53, Lafayette (1978).
26. Knoll, G. F. Radiation Detection and Measurement, 3rd ed. Ch 3 & 8 &9 (John Wiley and Sons 2000).
27. Birks, J.B. The Theory and Practice of Scintillation Counting. (Pergamon press Ltd 1964) https://doi.org/10.1016/B978-0-08-010472-0.50004-5
28. Lawrence, E. O. & Livingston, M. S. The Production of High Speed Light Ions Without the Use of High Voltages. Phys. Rev. 40(1), 19-35 (1932). https://link.aps.org/doi/10.1103/PhysRev.40.19
29. Chadwick, J. The Cyclotron and its Applications*. Nature 142, 630–634 (1938). https://doi.org/10.1038/142630a0
30. Mann, W. Recent Developments in Cyclotron Technique. Nature 143, 583–585 (1939). https://doi.org/10.1038/143583a0
31. Michaelis, E. Cyclotrons of all shapes and sizes. Nature 257, 270–271 (1975). https://doi.org/10.1038/257270a0

32. Alfassi, Z., Zlatin, T. & German, U. Simultaneous measurement of gamma-rays and neutron fluences using a HPGE detector. J Radioanal Nucl Chem 268, 237–241 (2006). https://doi.org/10.1007/s10967-006-0186-6
33. Walg J., Feldman J., Izarzar A., Rodinianski A., Mishani E. & Orion I., Cyclotron-produced neutrons measurements using Chlorine activation, Nuclear Inst. and Methods in Physics Research B 503, 1-5 (2021). https://doi.org/10.1016/j.nimb.2021.07.001.
34. Stöcklin, G. & Pike, V. W. Radiopharmaceuticals for Positron Emission Tomography Methodological Aspects (Kluwer Academic Publishers 1993).
35. web site http://www.nucleide.org/
36. Rostampour, M. et al. Experimental study and simulation of ^{63}Zn production via proton induce reaction. Applied Radiation and Isotopes 136, 32-36 (2018). https://doi.org/10.1016/j.apradiso.2018.02.005.
37. Szelecsényi, F. et al. Evaluated cross section and thick target yield data bases of Zn+p processes for practical applications. Applied Radiation and Isotopes 49(8), 1005-1032 (1998). https://doi.org/10.1016/S0969-8043(97)10103-8.

Supplementary information

To ascertain signal detectability for the measurements reported in the results and discussion section, we implemented the method of limits-of-detectability as described in the book "Radiation Detection and Measurement" (chapter 3 section VI)[26]. An example for statistical calculations of the Am-241 results (06-Feb-2019):

$\text{Mean} = 3692067.74$

$\sigma = 1795.51$

$L_C = 2.326 \cdot \sigma = 2.326 \cdot 1795.51 = 4176.359$

$\text{Mean} - L_C = 3692067.74 - 4176.359 = 3687891.38$

$$\%L_C = \left(1 - \frac{\text{Mean} - L_C}{\text{Mean}}\right) \cdot 100\% = \left(1 - \frac{3692067.74\text{-}4176.359}{3692067.74}\right) \cdot 100\% = 0.11\%$$

According to this calculation, if a change is greater than 0.11%, the signal exceeded the critical level and it is a reliable result.

$\text{dip} = 3679900$

$\text{Mean} = 3692067.74$

$\sigma = 1795.51$

$$\%\sigma = \frac{1795.5}{3692067.7} \cdot 100\% = 0.049\%$$

$$number\ of\ \sigma = \left(\frac{\%decrease}{\%\sigma}\right) = \left(\frac{0.38\%}{0.049\%}\right) = 7.75\sigma$$

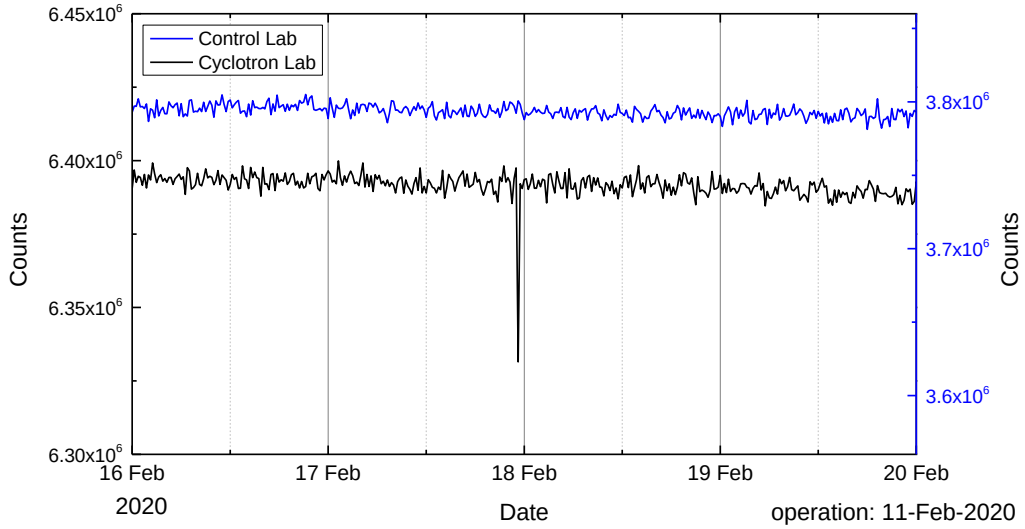

Figure 9. Results of Thorium system, as shown in Figure 3, compared to control lab similar system results.